Soft Matter

PAPER

View Article Online
View Journal | View Issue

Cite this: *Soft Matter*, 2014, **10**, 738

Self-assembling peptides form nanodiscs that stabilize membrane proteins

Søren Roi Midtgaard,[ab] Martin Cramer Pedersen,[b] Jacob Judas Kain Kirkensgaard,[b] Kasper Kildegaard Sørensen,[a] Kell Mortensen,[b] Knud J. Jensen*[a] and Lise Arleth*[b]

Received 24th June 2013
Accepted 24th October 2013

DOI: 10.1039/c3sm51727f

www.rsc.org/softmatter

New methods to handle membrane bound proteins, *e.g.* G-protein coupled receptors (GPCRs), are highly desirable. Recently, apoliprotein A1 (ApoA1) based lipoprotein particles have emerged as a new platform for studying membrane proteins, and it has been shown that they can self-assemble in combination with phospholipids to form discoidal shaped particles that can stabilize membrane proteins. In the present study, we have investigated an ApoA1 mimetic peptide with respect to its solution structure when in complex with phospholipids. This was achieved using a powerful combination of small-angle X-ray scattering (SAXS) and small-angle neutron scattering (SANS) supported by coarse-grained molecular dynamics simulations. The detailed structure of the discs was determined in unprecedented detail and it was found that they adopt a discoidal structure very similar to the ApoA1 based nanodiscs. We furthermore show that, like the ApoA1 and derived nanodiscs, these peptide discs can accommodate and stabilize a membrane protein. Finally, we exploit their dynamic properties and show that the 18A discs may be used for transferring membrane proteins and associated phospholipids directly and gently into phospholipid nanodiscs.

1 Introduction

Membrane proteins are abundant and crucial for the functioning of biological cells; it is estimated that up to 30% of the human genome codes for membrane proteins[1] and that membrane proteins are central targets for approximately 50% of all medical drugs.[2] Unfortunately, structural and functional studies of membrane proteins remain a challenge due to difficulties in their handling. An important consequence of this is the fact that membrane proteins are significantly underrepresented in the protein data bank (PDB), where only 792 out of the 94 715 structures correspond to membrane proteins (as of October 2012).

This problem is widely acknowledged and has been a scientific driver for major recent breakthroughs in the methods and procedures for membrane protein crystallization[3] as well as for the instrumentation of synchrotron-based X-ray protein crystallography.[4–6] In turn, this has led to an increased understanding of several protein complexes from the important class of G-protein coupled receptors[3] (GPCRs), for which the 2012 Nobel prize in Chemistry was given to Brian Kobilka and Robert Lefkowitz.

Despite these breakthroughs, stabilization and handling of membrane proteins are still considered major challenges and good methods for these tasks are very much needed. In the last decade, several lipoprotein based methods have been proposed for solving exactly this problem in biophysical and functional studies,[7] and the present work should be seen in this context.

The lipoproteins used for this purpose were derived from naturally occurring protein analogues and in particular from the amphipathic 243 amino acid long Apolipoprotein A1 (ApoA1) which is the main constituent in high density lipoproteins (HDLs), the carriers of so-called "good" cholesterol. An inverse relationship between HDL levels and the risk of coronary artery disease and atherosclerosis is well established in transgenic mice, rats and to a certain extent humans.[8,9] This has prompted the study of several ApoA1 mimetic peptides.[10–15] These peptides have been studied in detail with regard to their lipid affinity and atheroprotective properties. Phase 1 trials of one mimetic peptide show improvement in the HDL quality when administered *in vivo*.[16]

The structure of the lipid–peptide complexes has not been studied as extensively as their *in vivo* properties. However, it is well known that ApoA1 by itself can form discoidal particles when reconstituted with phospholipids,[17] and there is accumulating evidence that some of these mimetic peptides also form discoidal shaped particles when associated with lipids.[10,18–20] The structural studies made on lipid–peptide particles have so far mainly been performed on different variants of an 18 amino acid long amphipathic α-helical peptide of the so-called class A type,[21] in the following referred to as 18A. This peptide is also the focus of the present work and was

[a]*Department of Chemistry, University of Copenhagen, Denmark. E-mail: kjj@chem.ku.dk*

[b]*Niels Bohr Institute, University of Copenhagen, Denmark. E-mail: arleth@nbi.ku.dk*

assembled synthetically to mimic the *in vivo* properties of ApoA1.[10,18] Hence, it has approximately the same dimensions and structure as the single alpha helices in the original ApoA1 protein.[22] The lipid–peptide particle structure of the 18A and similar systems have previously been probed by size exclusion chromatography (SEC), electron microscopy (EM), mass spectrometry (MS) with crosslinking experiments and proton and phosphate nuclear magnetic resonance (NMR) spectroscopy.[10,18–20] In combination, these studies suggest that the resulting particle from the 18A peptide mixed with phospholipids is a disc with a diameter of ~7 nm. The peptides are expected to align themselves pair-wise in an antiparallel head to tail fashion around the outer perimeter of the disc. This way the hydrophobic lipid tails are screened from the surrounding solvent. Despite these measurements providing detailed information on the structure of the peptide and the binding to the lipids, the evidence for the overall structure of the discs in solution is still missing. This is one aspect we address in this work, and it is a necessary step towards developing the particles into a platform for the handling of membrane proteins.

A number of different approaches for the incorporation and stabilization of membrane proteins exist. An approach that has had some success in the last decade is the so-called bicelles.[23] Generally, these consist of two kinds of phospholipids or other amphiphilic molecules of different hydrophobic chain lengths. Under the right conditions, these mixed micelles segregate locally to form discoidal shaped bilayer based micelles also referred to as bicelles.[24] Incorporation of membrane proteins into these has shown some success in stabilizing and crystallizing membrane proteins.[24,25]

The usage of the ApoA1 based discs for this same purpose has developed more recently and has been promoted under the name "nanodiscs".[26] A steadily increasing number of membrane protein types have been incorporated into these discs, and the discs themselves have also been the subject of a number of studies.[27] It is the general experience that membrane proteins are more stable in nanodiscs than in bicelles, probably due to the more native membrane like environment, but the bicelle based reconstitution is significantly simpler from a sample handling point of view.

Therefore, one of the central goals of the present work has been to investigate if the amphipathic 18A peptide based discs would provide a good compromise between the bicelle-system and the ApoA1 based system that would conserve the flexibility of the bicelle system while also containing the native membrane-like environment of the ApoA1 based system. To answer these questions, we started by investigating the "empty" lipid–peptide discs formed by the amphipathic 18A peptide in combination with 1,2-dimyristoyl-*sn-glycero*-3-phosphocholine (DMPC). This revealed the solution structure of the disc in detail and provided a foundation for the later studies with membrane proteins. The structural SAXS/SANS analyses were complemented by a coarse-grained molecular dynamics simulation study. This qualitatively reproduced the experimental findings using a very simple system with only a few parameters. These simulations provided valuable insight into the formation of the discs and the dynamical behaviour of systems, both of which were fed back into the modeling and interpretation of the scattering data. This leads to a better understanding of the system and resulted in yet a better model fit to the experimental data still in good accordance with expectations from the literature.[28]

We proceeded by investigating the capacity of the 18A:DMPC discs for accommodating and stabilizing membrane proteins. This was inspired by the results for the ApoA1 based nanodisc systems and their capacity to stabilize a range of membrane proteins.[29] In this context, it was rewarding to observe that not only was it possible to incorporate membrane proteins into the 18A:DMPC discs but also the stability of the membrane protein was greatly enhanced compared to a traditional detergent. Other peptide based detergents (peptergents) have been reported to stabilize a variety of different membrane proteins.[30–36] However, none of them have as complex an amino acid sequence or are as long as the 18A peptide. Furthermore, none of these peptides or other similar synthetic polymers that have been shown to stabilize membrane proteins in solution[37,38] have previously been tested or characterized with added lipids to form ApoA1 disc-like structures with incorporated membrane proteins. Light scattering was used to monitor the time dependence of the 18A:DMPC system with and without bR. This showed that the discs grew in size with a dependence of the growth rate on the storage temperature and whether a membrane protein was present or not.

Finally, we found that an 18A peptide disc could be used as a vehicle for reconstitution of a membrane protein directly into a traditional "nanodisc", hence avoiding the classical detergent based reconstitution.[7] At present, successful reconstitution of membrane proteins into nanodiscs is a major bottleneck for further exploitation of the nanodisc platform. The added advantage provided by the 18A discs may help solving this problem and to our knowledge, no other system has exhibited the same compatibility with the nanodisc system as we show here for the 18A:DMPC discs.

2 Methods

2.1 Experimental

2.1.1 General. All water used was of MilliQ grade with a resistance of 18.2 MΩ. For the peptide synthesis, amino acids, coupling reagents, DIEA, piperidine, DMF and NMP were all obtained from Iris Biotech GmbH and Sigma-Aldrich. All other chemicals were obtained from Sigma-Aldrich unless otherwise noted. Superdex 200 and Ni-NTA columns were run on Äkta systems according to the manufacturer's instructions. Columns and systems were obtained from GE-Healthcare.

2.1.2 Peptide synthesis. The basic sequence for the synthetic peptide has the following 18 amino acid sequence DWLKAFYDKVAEKLKEAF and is acetylated at the N-terminus and amidated at the C-terminal. The N-terminal acetylation removes a positive charge and introduces a carbonyl that has been shown to stabilize the α-helical structure of the peptide.[39] In the literature, this peptide is known as 18A (Ac-18A-NH_2) or alternatively as 2F due to the two phenylalanine residues present in the sequence.[40] The 18A peptide was prepared by

solid-phase peptide synthesis on an automated peptide synthesizer (Syro II, Biotage) on a TentaGel S Rink Amide 0.24 mmol g^{-1} (Rapp Polymere GmbH) resin with 9-fluorenylmethyloxycarbonyl (Fmoc) for protection of Nα-amino groups. Side-chain protecting groups were *tert*-butyl for Tyr, Asp, Glu and *tert*-butyloxycarbonyl for Lys and Trp. Nα-Fmoc amino acids (5.0 equivalents) were coupled using *N*-[(1*H*-benzotriazol-1-yl)(dimethylamino)methylene]-*N*-methylmethanaminium hexafluorophosphate N-oxide (HBTU) in 4.75 equivalents, 1-hydroxy-7-azabenzotriazole (HOAt) in 5 equivalents and *N*,*N*-diisopropylethylamine (DIEA) in 9.75 equivalents as coupling reagents in dimethylformamide (DMF) for 2 × 120 min at room temperature (RT). Nα-Fmoc deprotection was performed using 40% piperidine in DMF for 3 min, followed by using piperidine 2 times in DMF (1 : 4) for 15 min. In between couplings and deprotection, the resin was washed 3 times with NMP, DCM and subsequently 3 times with NMP. The peptides were released from the solid support by treatment with trifluoroacetic acid (TFA), triethylsilane (TES) and H_2O (95 : 2 : 3) for 2 h. The TFA solutions were concentrated by nitrogen flow and the compounds were precipitated with diethyl ether to yield the crude product. The crude peptide was purified by RP-HPLC (Dionex Ultimate 3000 system) with a preparative C18 column (FeF Chemicals, 200 Å 10 μm C18 particles, 2.1 × 200 mm) using the following solvent systems: water containing 0.1% TFA (solvent A) and acetonitrile containing 0.1% TFA (solvent B). Gradient elution from solvent A to B (0–10 min: 10% to 30%; 10–30 min: 30% to 100%) was applied at a flow rate of 10 ml min^{-1} and the column effluent was monitored by the UV absorbance at 215 nm and 254 nm simultaneously. The purity of the peptide was evaluated by analytical HPLC, and the identification was carried out by electrospray ionization mass spectrometry (ESI-MS) (MSQ Plus Mass Spectrometer, Thermo).

2.1.3 Bacteriorhodopsin purification. Bacteriorhodopsin (bR) was produced and purified according to previously published reports.[41,42] Briefly, salt media containing per 1 L H_2O 250 g NaCl, 20 g $MgSO_4 \cdot 7H_2O$, 10 g peptone (Oxoid), 3 g trisodium citrate and 2 g KCl was inoculated with *H. salinarium*. After 5–6 days of growth at 40 °C and illumination with a 500 W lamp, the cells were pelleted and washed in salt buffer containing per 1 L H_2O: 250 g NaCl, 20 g $MgSO_4 \cdot 7H_2O$ and 2 g KCl. The cells were resuspended in 25 ml MQ H_2O per gram of cells. DNase was added, and the solution was left stirring overnight at 4 °C. The cell debris was spun down, the supernatant was transferred to centrifuge tubes, and the membranes were pelleted at 54 000*g* for 1 h. The supernatant was discarded, and the pellet was resuspended in MQ H_2O and spun down further two times to remove impurities. Isolated membranes were resuspended in a minimum amount of MQ H_2O and carefully layered on top of a sucrose gradient consisting of a step gradient of 30%, 40% and 50% of sucrose dissolved in STED buffer containing 10 mM Tris–HCL pH 7.5, EDTA 1.5 mM and DTT 0.5 mM. The gradient was centrifuged overnight at 200 000*g* to reach equilibrium. Next day, the band containing the purple membrane was extracted and dialyzed against 25 mM phosphate buffer pH 7.4 to remove the sucrose. Octyl glucoside (OG, Applichem) was added to the purple membrane sample to obtain a weight ratio of detergent to bR of ~20, and the sample was diluted to obtain a final OG concentration of 40 mM. The solution was lightly sonicated, left under gentle agitation at room temperature overnight and protected from light. After solubilization, the bR was loaded onto a Superdex 200 column equilibrated in 25 mM phosphate buffer pH 7.4 and 40 mM OG. Fractions containing monomeric bR were collected, concentrated, flash frozen and stored at −80 °C until further use.

2.1.4 Peptide disc self-assembly. The empty peptide discs (18A:DMPC) were formed as described previously.[19] Peptide and DMPC were dissolved in methanol, mixed in 1 : 1 ratio (w/w) and dried under a stream of nitrogen. The sample was lyophilized overnight to remove any residual methanol. 5 mM KH_2PO_4 was added to the peptide–lipid film to yield a final peptide concentration of 3.3 mM. The sample was subsequently incubated at 37 °C overnight. The assembled discs were applied to a Superdex 200 column equilibrated in phosphate buffered saline (PBS). In the dilution on the gel filtration column, the concentration of detergent decreased to below the CMC value, and the detergent was thereby removed. Peak fractions from the SEC were collected and used immediately.

bR loaded discs (18A:DMPC:bR) were prepared by adding purified and concentrated bR in 25 mM phosphate buffer pH 7.4 and 40 mM OG to the dry peptide–lipid film to a final peptide concentration of 3.3 mM. This was left to incubate at room temperature for 15 min and then applied to a Superdex 200 column equilibrated in PBS. Peak fractions were collected and used immediately. A typical chromatogram is shown in Fig. 6.

2.1.5 Nanodisc belt purification. The ApoA1 based belt used in this study was the Membrane Scaffold Protein-1-D1 (MSP1D1) prepared by Sligar and co-workers.[7] The protocol used to purify the MSP1D1 protein is a variant of the protocol previously published for the purification of recombinant Membrane Scaffold Protein (MSP) constructs. Briefly, *E. coli* cells were grown in Terrific Broth (TB) media and induced with 1 mM IPTG (final concentration) at OD (600 nm) = 0.6–0.8 for 4 hours. The cells were resuspended in 20 mM phosphate buffer, pH 7.4 and 1% Triton X-100 with 3 ml of buffer to 1 g of cells. These were opened by sonication. Cell debris was pelleted by centrifugation. A Ni-NTA column (1 ml resin for 10–25 mg of MSP) was equilibrated in 40 mM phosphate buffer, pH 7.4 and 1% Triton X-100, and the supernatant was applied to the column. The column was washed in sequence with 3–5 column volumes of buffers containing: wash buffer 1: 40 mM Tris–HCl pH 8.0, 0.3 M NaCl and 1% Triton X-100. Wash buffer 2 : 40 mM Tris–HCl pH 8.0, 1 M NaCl, 50 mM sodium cholate and 20 mM imidazole. Wash buffer 3: 40 mM Tris–HCl pH 8.0, 0.3 M NaCl and 50 mM imidazole. MSP was eluted from the column with 40 mM Tris–HCl pH 8.0, 300 mM NaCl and 400 mM imidazole. The protein was dialyzed against 20 mM Tris pH 7.4 and 100 mM NaCl. MSP1D1 was subsequently concentrated, lyophilized and frozen until further use.

2.1.6 Nanodisc formation from peptide discs. The bR loaded peptide discs and purified MSP1D1 were prepared as described above. Purified MSP1D1 was added to the 18A:DMPC:bR discs in a molar ratio of 90 DMPC molecules to

one MSP1D1 molecule. This mixture was left to incubate for 1 h at room temperature. The sample was applied to a prepacked 1 ml Ni-NTA column pre-equilibrated in 20 mM Tris pH 7.4 and 100 mM NaCl. After washing, the retained sample was eluted with the same buffer containing 500 mM imidazole, and the eluate was subsequently applied to a Superdex 200 equilibrated in 20 mM Tris pH 7.4 and 100 mM NaCl. Fractions were monitored by UV absorption at 280 nm and 550 nm to measure the total protein and bR specific absorption, respectively. Peak fractions containing bR were analyzed by SDS-PAGE and subsequently silver stained to check the protein contents of the obtained sample. The only major bands found in the sample corresponded to bR and MSP1D1 (data not shown).

2.1.7 Light scattering. Simultaneous dynamic light scattering (DLS) and static light scattering (SLS) measurements were performed on a Brookhaven Instruments Corporation instrument using a laser wavelength of $\lambda = 632.8$ nm. Time-resolved measurements were conducted in 7 min windows for 10 °C and 20 °C measurements and in 1 min window for 30 °C measurements. The initial size of the particles was determined from the recorded DLS autocorrelation functions using the second order cumulant method analysis included in the instrument software (9KDSLW). Evolution of the size of the particles could be monitored by the total SLS intensity due to the direct relationship between the Rayleigh ratio, R_θ, and the molecular mass, M:

$$R_\theta = \frac{i_\theta}{I_0}\frac{r^2}{1+\cos^2\theta} = KCM$$

where i_θ is the scattering intensity at angle θ, I_0 is the laser intensity, r is the detector distance from the sample, C is the protein concentration, and K is the light scattering optical constant related to the polarizability of the particles defined as:

$$K = \frac{4\pi^2 n_0^2 (\mathrm{d}n/\mathrm{d}C)^2}{N_A \lambda_0^4}$$

where n_0 is the solvent refraction index, λ_0 is the wavelength of the laser source in vacuum, N_A is the Avogadro number and the ratio $\mathrm{d}n/\mathrm{d}C$ is the increment of the refractive index. Because the particles may change their composition over time, there is likely a subtle change in the refractive index during the experiment. This does not affect the general trend seen in the experiments. Because all the parameters were held constant, a direct relationship between the mass of the particle M and the measured intensity i_θ could be obtained. This direct relationship holds for Rayleigh scattering,[43] meaning that the wavelength used should be much larger than the studied particle. In practice, this condition is fulfilled at a ratio of ~20, meaning that the maximum size that could be monitored in this way was ~30 nm. The data are presented as a plot (Fig. 7) of the normalized particle mass (NM), defined as $\mathrm{NM} = I(t)/I(t=0)$, where $I(t)$ is the measured intensity at time t, and $I(t=0)$ is the measured intensity at the first measurement. The diameter of the particles was monitored by DLS analysis and did not exceed a particle diameter of ~30 nm. The measured samples were analyzed by UV 280 nm absorption to study whether or not peptide had precipitated during the course of the measurement. No change was observed (see the Results section).

2.1.8 UV/VIS absorption measurements. All light absorption measurements used for determining the protein content and bR stability were performed on a Nanodrop 1000 spectrometer (Thermo Fisher Scientific) using a path length of 1 mm. The stability of bR could directly be monitored by the specific absorbance at 550 nm, as this disappears, when bR is denatured. The whole spectrum was monitored to make sure that there was no interference from scattered light.

2.1.9 SAXS/SANS data collection. SAXS and SANS data for the 18A:DMPC disc were obtained simultaneously at a combined beamtime at the European Synchrotron Radiation Facility (ESRF) and Institut Laue Langevin (ILL) in Grenoble, France. The SAXS data were recorded at the beamline ID14-3, and absolute scale calibration was performed with bovine serum albumin (BSA) as a reference. The SANS data were recorded at the D11 instrument, and H_2O was used for absolute scale calibration. In both cases, the collected data were measured at 20 °C in D_2O. The normalized 2D data were azimuthally averaged and background subtracted to yield the scattering intensity, $I(q)$, where the scattering vector q is defined by $q = 4\pi/\lambda \sin(\theta)$, where θ is half the scattering angle and λ is the wavelength of the incoming beam. To be sure that the samples measured by SAXS and SANS were exactly similar, one sample was prepared, divided in two, and measured at the same time with X-rays and neutrons at the respective facilities in Grenoble. By having data from SAXS and SANS contrast situations, the amount of information about the samples was increased. This significantly reduced the number of possible models fitting both datasets, thereby increasing the certainty of the refined model and deduced parameters. SAXS data for the 18A:DMPC:bR loaded discs and for screening the polydispersity of the SEC peaks were obtained at MAXLab in Lund, Sweden at the recently commissioned beamline I911-4 (MAXSAXS).

2.2 Computational methods

2.2.1 Modeling of small-angle scattering data. Small-angle neutron and X-ray scattering data were obtained for the 18A:DMPC system. As motivated by the coarse-grained simulation results (see the description later), we decided to try to model the 18A:DMPC particles as discoidal structures. This is in agreement with previous interpretations of the structure.[19] The utilized model is an analytical description based on a previously outlined strategy for describing disc-shaped particles,[44–46] which in turn is based on the fundamental principles for refining models from small-angle scattering data.[47] Much in line with these references, our model relies on invoking molecular constraints, which allow for simple and efficient parameterization of the geometric description for the peptide–lipid particles in terms of the number of involved lipids and peptides. The derived analytical model expression presented below was fitted to the scattering data using a modified version of the Levenberg–Marquardt algorithm[48] applied to a χ^2-minimization. Furthermore, an independent control was performed using the Broyden–Fletcher–Goldfarb–Shanno (BFGS) algorithm.[49–53] The Levenberg–Marquardt algorithm has previously been described in the context of small-angle scattering,[47] and the source codes

for both algorithms are available in the literature.[54] The presented confidence intervals were estimated using the profile likelihood framework– thus, the 95% – confidence interval corresponds to the values of a given parameter, for which a minimum with a χ^2 no larger than that of the fitted minimum plus 3.84 could be found – in accordance with the fundamental properties of the χ^2-distribution.

Disc parameterization. For the purpose of analyzing the small-angle scattering data obtained for the 18A:DMPC particles, the discs can be represented as a combination of stacked cylinders, each representing a given part of the disc.[45,46] In total, four different contrasts are represented in our model: the peptide belt, the lipid headgroups, the lipid hydrophobic alkyl chains and the hydrophobic methyl groups situated at the end of the lipid tails. The model is illustrated in Fig. 1.

By systematic incorporation of molecular constraints, including *a priori* knowledge of the chemical composition of the peptides and the lipids, the model of a single disc can be parameterized by the number of lipids per disc, n_l, the area per lipid headgroup, a_{head}, the width and the height of the peptide belt surrounding the lipid bilayer disc, d and h, respectively, and finally the partial specific molecular volumes of a single peptide and a single lipid, ν_p and ν_l, respectively. The height of the peptide belt, h, was fixed at 24 Å during the fitting process in accordance with previous findings.[45,46] These parameters, in combination with the molecular constraints of the model, allow for deriving the full geometrical description of the 18A:DMPC disc and consequently the scattering profile of the entire disc. The orientationally averaged scattering profile from a single disc is given by:

$$\begin{aligned} I_{disc}(q) = \frac{1}{2}\int_0^{\pi} \sin(\alpha)\big(&V_{belt}\Delta\rho_{belt}A_{belt}(q,\alpha) \\ &+ V_{head}\Delta\rho_{head}A_{head}(q,\alpha) \\ &+ V_{tail}\Delta\rho_{tail}A_{tail}(q,\alpha) \\ &+ V_{meth}\Delta\rho_{meth}A_{meth}(q,\alpha)\big)^2 d\alpha \end{aligned}$$

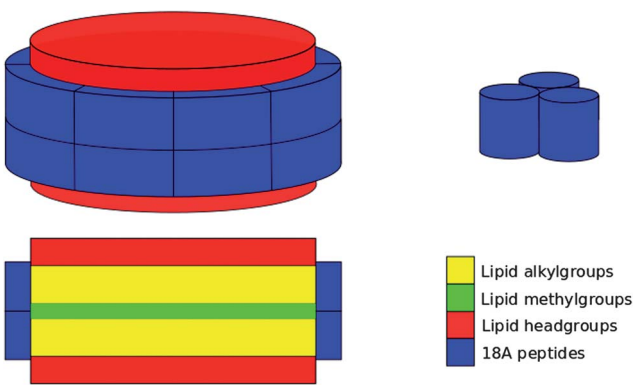

Fig. 1 Upper left: the top view of the geometrical 18A:DMPC-disc model used for the SAXS/SANS analysis. The different colors represent parts of the disc with differing excess scattering length densities. Lower left: the cross-section of the same model showing the internal layers. Upper right: a geometrical representation of the 18A peptide trimer as it is expected to appear in solution.

where the different form factor amplitudes, A_{belt}, A_{head}, A_{tail} and A_{meth}, are based on the form factor for a circular cylinder.[47,55] The volumes, V_{belt}, V_{head}, V_{tail} and V_{meth}, as well as the excess scattering length densities, $\Delta\rho_{belt}$, $\Delta\rho_{head}$, $\Delta\rho_{tail}$ and $\Delta\rho_{meth}$, can be calculated from the geometry of the discs combined with the knowledge of the chemical composition and the partial specific molecular volumes of the various parts of the complex. We obtain:

$$\begin{aligned} V_{head} &= n_l\nu_{head} \\ V_{tail} &= n_l\nu_{tail} \\ V_{meth} &= n_l\nu_{meth} \\ V_{belt} &= \pi dh\left(d + \sqrt{2n_l a_{head}/\pi}\right) \end{aligned}$$

Size distribution of the 18A:DMPC discs. Due to the inherent dynamic nature of the self-assembly process of the lipids and peptides, the measured sample was expected to be polydisperse to some degree. As will be explained later, this was suggested by the simulations (see the Results section Fig. 3) and confirmed by the difference of SAXS data obtained on all fractions across the size exclusion peak seen in Fig. 6 (SAXS data not shown). This prompted us to adopt a polydispersity into the model, so the total intensity was modeled as a distribution of peptide discs, where the amount of lipids in the discs followed a Gaussian distribution, whereas the width of the peptide belt, d, was kept identical for each peptide disc, regardless of the size. This implies that the final model depends on the mean number of lipids in the peptide discs, $\bar{n}$, as well as the standard deviation, σ, of the Gaussian distribution. For practical purposes, the Gaussian distribution was only evaluated in the interval $[\bar{n} - 3\sigma, \bar{n} + 3\sigma]$ and truncated for unphysical negative values of the number of lipids. Incorporating an ellipticity of the discs as done in previous work[45,46] would most likely also allow for describing the experimental data. However, since the above points are towards the polydispersity rather than the ellipticity as the dominating factor and since it is notoriously difficult to extract parameters about both polydispersity and ellipticity from small-angle scattering data, we decided to keep the model simple and only include the polydispersity.

Peptide trimer. An equilibrium is expected to exist between 18A peptides forming coiled–coil structures and nanodiscs due to the dynamic nature of the system. As will be described in the Results section, the simulations indicate the possible presence of a small subpopulation of peptide trimers in solution. The formation of this coiled–coil trimer was driven by the hydrophobic collapse of the peptides. To include these trimeric structures in the modeling, we estimate that a peptide monomer can be described as a cylinder with a circular cross-section radius, r, of 5.0 Å. The length of the cylinders modeling the peptide trimers, l, follows trivially from the partial specific molecular volume of the object, as $l = \nu_{pept}/(\pi r^2)$. The scattering from a trimer of peptides organized as depicted in Fig. 1 can now be described by the form factor amplitudes of a cylinder multiplied by appropriate phase factors representing their position relative to each other. The full expression is given by:

$$I_{\mathrm{trim}}(q) = \frac{1}{4\pi}\int_0^{\pi} \mathrm{d}\alpha\, \sin(\alpha) \int_0^{2\pi} \mathrm{d}\beta \big| \nu_{\mathrm{pept}}\Delta\rho_{\mathrm{belt}} A_{\mathrm{pept}}(q,\alpha)\psi_1 + \nu_{\mathrm{pept}}\Delta\rho_{\mathrm{belt}} A_{\mathrm{pept}}(q,\alpha)\psi_2 + \nu_{\mathrm{pept}}\Delta\rho_{\mathrm{belt}} A_{\mathrm{pept}}(q,\alpha)\psi_3 \big|^2$$

where the ψ's are the appropriate phase factors, and the partial specific molecular volume of the peptide, ν_{pept}, and the excess scattering length density of the peptide, $\Delta\rho_{\mathrm{pept}}$, are assumed to be identical to those of the peptides in the protein belt surrounding the peptide disc. Finally, the form factor amplitudes, A_{pept}, are the previously mentioned form factor amplitudes of a cylinder with the given dimensions. The $|\ldots|$ denotes the modulus of the complex expression within. The applied excess scattering length densities are based on the values for the total scattering length of the various components of the 18A-discs presented in Table 1. Furthermore, in order to accurately model the ratio between the amounts of peptides in discs and in trimers, a parameter corresponding to the overall number of lipids per peptide in the sample, ε, was fitted. In conclusion, the following model was fitted on an absolute scale to the experimental scattering intensity:

$$I(q) = n_{\mathrm{trim}} I_{\mathrm{trim}}(q) + n_{\mathrm{disc}} \int_{\bar{n}-3\sigma}^{\bar{n}+3\sigma} \mathrm{d}N I_{\mathrm{disc},N}(q) \frac{\mathrm{e}^{-\frac{(N-\bar{n})^2}{2\sigma^2}}}{\sigma\sqrt{2\pi}}$$

where n_{trim} and n_{disc} denote the particle number densities of the different aggregates, and $I_{\mathrm{disc},N}(q)$ is $I_{\mathrm{disc}}(q)$ for a peptide disc with N lipids. These particle number densities can be deduced from the concentration of the peptides, the lipid-to-peptide ratio in the discs, φ, the number of lipids per peptide in the sample, ε, and the mean number of peptides per peptide disc, η, which can be derived from the properties of the Gaussian distribution and the geometry of the model of the peptide disc:

$$n_{\mathrm{trim}} = \left(1 - \frac{\varepsilon}{\varphi}\right)\frac{n_{\mathrm{pept}}}{3}$$

$$n_{\mathrm{disc}} = \frac{\varepsilon}{\varphi}\frac{n_{\mathrm{pept}}}{\eta}$$

where n_{pept} denotes the overall number density of peptides in the sample, which was determined experimentally.

2.2.2 Coarse-grained molecular dynamics simulations. We have performed coarse-grained molecular dynamics simulations of generic peptide–lipid assemblies using the approach developed by Cooke and Deserno.[56,57] The model has already been used in a number of studies, investigating various aspects of lipid self-assembly and membrane remodelings on long length and time scales.[56–59] The key idea of the model is to create a fast simulation setup by using an implicit solvent representation, *i.e.* the solvent is not explicitly represented as particles, but included by an effective potential governing the self-assembly of the system. In practice, groups of atoms are represented in a coarse fashion as a single bead, and beads of hydrophobic or hydrophilic nature are suitably connected to represent the overall geometric features of lipids and peptides, respectively, see Fig. 2. The implementation details are outlined below, and further details can be found in the original papers.

Following a setup for modeling a very similar system,[59] we model a lipid with 4 beads, one hydrophilic headgroup bead and three hydrophobic tail beads, and each peptide as a cylinder of hexagonally arranged beads around a central chain, see Fig. 2. The self-assembly of the model lipids can be tuned geometrically by varying the size of the headgroup bead relative to the tail beads, thus controlling the resulting membrane curvature. Here, we use model lipids, which preferably form a flat membrane as DMPC would. The model peptides are 6 beads long and mimic the hydrophilic/hydrophobic characteristics of the 18A-peptide side chains by representing 1/3 of the surface area as hydrophobic *via* two rows of beads, as shown in Fig. 2. The peptide–lipid length ratio 6 : 4 reflects the synthesized peptide length ratio with an average peptide length of ~32 Å and an approximate lipid length of 20 Å. In the simulations, all

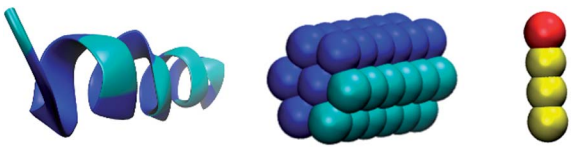

Fig. 2 Model representations and color codes of the lipids and peptides investigated *via* the coarse-grained molecular dynamics simulations. Left: cartoon representation of the 18A peptide with hydrophilic/hydrophobic side chain regions colored blue/cyan respectively. The hydrophobic side chains form a patch running along the peptide covering approximately 1/3 of the area. Middle: coarse-grained version of the peptide used in the simulations. Right: coarse-grained lipid. Hydrophilic/hydrophobic beads on the peptides are represented in blue/cyan respectively. The hydrophilic headgroups in the lipids are represented in red and the hydrophobic tails are colored yellow.

Table 1 Molecular weights (M_w), partial specific molecular volumes (ν), chemical composition, scattering lengths (b_x and b_n for X-rays and neutrons respectively) and the corresponding scattering length densities (ρ_x and ρ_n) of the various components of the 18A:DMPC model. The scattering lengths associated with neutron scattering are only representative, when the sample is in 100% D_2O due to hydrogen–deuterium-exchange. The presented values for the partial specific molecular volumes are the refined values, and consequently, the scattering length densities are based on these values, using $\rho = b/\nu$

Component	M_w, [Da]	ν, [Å^3]	Composition	b_x, [cm]	b_n, [cm]	ρ_x, [cm Å^{-3}]	ρ_n, [cm Å^{-3}]
18A-peptide	2240	2430	$C_{108}H_{160}N_{24}O_{28}$	3.32×10^{-10}	8.29×10^{-11}	1.37×10^{-13}	3.41×10^{-14}
Headgroup	311	316	$C_{10}H_{18}NO_8P$	4.62×10^{-11}	7.05×10^{-12}	1.46×10^{-13}	2.23×10^{-14}
Alkyl chains	337	676	$C_{24}H_{48}$	5.41×10^{-11}	-2.00×10^{-12}	8.00×10^{-14}	-2.96×10^{-15}
Methyl groups	30.1	108	C_2H_6	5.08×10^{-12}	-9.15×10^{-13}	4.70×10^{-14}	-8.47×10^{-15}
D_2O-buffer	20.0	30.0	D_2O	2.82×10^{-12}	1.91×10^{-12}	9.40×10^{-14}	6.37×10^{-14}

physical quantities are represented by dimensionless numbers, and we will briefly discuss the mapping of these to real length and time scales. All beads are set to have the same mass m, permitting the definition of a coarse-grained time unit $\tau = \sigma\sqrt{m/\varepsilon}$ denoting our units of energy and length, ε and σ, respectively. As our simulations basically utilize the same parameters as those utilized by Illya and Deserno,[59] the same considerations regarding mapping length, energy and time scales apply here. Most relevant is the fact that our length scale mapping derived from representing an on average 32 Å long peptide with 6 beads is $\sigma \sim 5.3$ Å and that the effective coarse-grained time scale is roughly $\tau_{\text{eff}} \sim 10$ ns. The latter is model dependent in a non-trivial way, see ref. 59 for further details. In the simulations, all bead sizes are controlled *via* a repulsive, truncated and shifted Lennard-Jones potential:

$$V_{\text{rep}}(r,b) = \begin{cases} 4\varepsilon\left[\left(\frac{b}{r}\right)^{12} - \left(\frac{b}{r}\right)^{6} + \frac{1}{4}\right] & \text{for } r \le r_{\text{c}} \\ 0 & \text{for } r > r_{\text{c}} \end{cases}$$

with $r_{\text{c}} = 2^{(1/6)}b$. Connected beads along each lipid chain are linked by a so-called FENE bond:

$$V_{\text{bond}} = -\frac{1}{2}\kappa_{\text{bond}} r_{\infty}^2 \log\left[1 - \left(\frac{r}{r_{\infty}}\right)^2\right]$$

with the stiffness $\kappa_{\text{bond}} = 30\varepsilon/\sigma^2$ and divergence length $r_{\infty} = 1.5\sigma$. A harmonic spring acting between the headgroup bead and the last bead of the chain straightens the lipids by controlling their stiffness:

$$V_{\text{bend}} = \frac{1}{2}\kappa_{\text{bend}}(r - 4\sigma)^2$$

where the bending stiffness is set to $\kappa_{\text{bend}} = 10\varepsilon/\sigma^2$. In the peptides, all horizontal, vertical and diagonal neighbour beads are connected by harmonic springs:

$$V_{\text{p}} = \frac{1}{2}\kappa_{\text{p}}(r - r_0)^2$$

with $\kappa_{\text{p}} = 200\varepsilon$ and $r_0 = 1.2\sigma$. This leads to a stiff, non-twisting and rigid structure. The final interaction is the attraction, which acts between all hydrophobic beads according to:

$$V_{\text{attr}}(r,b) = \begin{cases} -\varepsilon & \text{for } r < r_{\text{c}} \\ -\varepsilon\cos^2\left[\frac{\pi(r - r_{\text{c}})}{2\omega_{\text{c}}}\right] & \text{for } r_{\text{c}} \le r \le r_{\text{c}} + \omega_{\text{c}} \\ 0 & \text{for } r > r_{\text{c}} + \omega_{\text{c}} \end{cases}$$

This is an attractive potential with the potential depth ε and an interaction range set by the cohesion width ω_{c}. In the simulations, the hydrophobic beads are either the lipid tails or the hydrophobic peptide strips, thus, the interactions governing the self-assembly are the lipid–lipid, peptide–peptide and lipid–peptide interactions controlled by V_{attr} with separate values for the ω_{c} parameter termed ω_{ll}, ω_{pp} and ω_{pl} respectively. Thus, the modeling of the lipids and peptides effectively amounts to defining their geometric characteristics and mutual interaction parameters. Simulations are performed as constant volume (NVT ensemble) simulations using a Langevin thermostat with time steps $\delta t = 0.005\tau$ and a friction constant $\Gamma = \tau^{-1}$. Simulations are performed in a cubic box of side length $L = 60\sigma$ under periodic boundary conditions. The peptide concentration is set to 3 mM, close to the experimental value, and the ratio of lipids to peptides in the results shown here is 16 : 1 with each simulation containing 60 peptides and thus 960 lipids. All simulations are started from a random gas configuration using sequential force capping and run for a minimum of 200 000τ. Thus, each simulation effectively corresponds to at least 2 ms of real time. Simulations were run using the ESPResSo package[60] and simulation snapshots were all made with the VMD package.[61]

3 Results

3.1 The 18A:DMPC system

3.1.1 Molecular dynamics simulations. As mentioned in the Methods section, the key parameters dictating the self-assembly of the peptide–lipid mixtures are the mutual interaction parameters between lipids and peptides controlled by the cohesion width parameters ω_{ll}, ω_{pp} and ω_{pl}. We follow previously published reports[59] and fix the lipid–lipid interaction at $\omega_{\text{ll}} = 1.6$. This value defines the overall physical properties of the resulting membrane, in particular the temperature dependent phase behavior and membrane bending modulus. The full excursion of the (ω_{pp} and ω_{pl})-phase diagram including the temperature dependence generates a wealth of information. In the following, the general traits relevant for the specific system studied in the present work will be presented. In qualitative terms, the phase behavior can be described depending on whether the peptides prefer to associate more or less with lipids than themselves. However, for $\omega_{\text{lp}} < \omega_{\text{ll}}$ the peptides and lipids do not form combined aggregates which is in disagreement with our experiments: we know that there are both peptides (from the UV-absorbance) and lipids (from the negative contrast visible in the IFT from X-ray scattering) in the aggregates. Also, since the 18A peptides are designed with strong lipophilic character along the hydrophobic patch, the relevant part of the phase diagram is where $\omega_{\text{pl}} \sim \omega_{\text{ll}}$, thus we will focus on results from this part of the phase diagram and discuss the variation of ω_{pp} below. Furthermore, the experimental data presented here are obtained slightly below the DMPC fluid–gel transition temperature, and thus, we focus on the results with $k_{\text{B}}T = 1.0\varepsilon$, which corresponds to this in the lipid model for the chosen cohesion width.

In the relevant part of the phase diagram for this paper, discoidal peptide–lipid aggregates are formed in all simulations at $k_{\text{B}}T = 1.0\varepsilon$, an example of which is shown in Fig. 3. We observe two universal features in all simulations with formation of discoidal peptide–lipid aggregates. Firstly, a pronounced polydispersity of aggregate sizes as can be seen in Fig. 3, and secondly, the evolution of the size distribution over time is observed *via* fusion of aggregates. An example of a fusion event is illustrated in Fig. 4, where two smaller peptide–lipid aggregates fuse to form a discoidal aggregate. As shown later in the text, the rise of average aggregate size over time is consistent

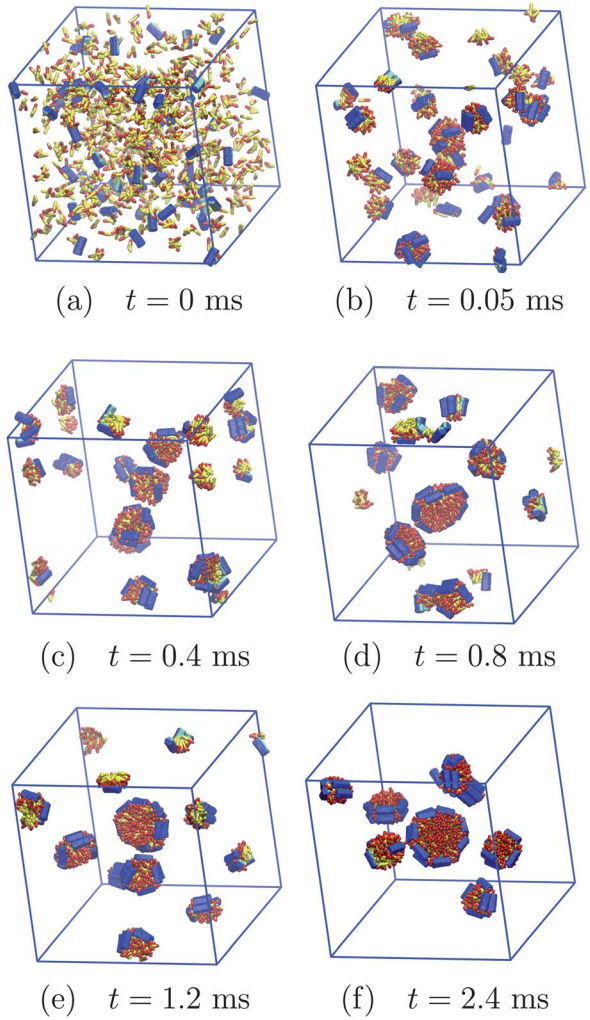

Fig. 3 Time evolution of simulation with interactions $\omega_{pp} = 0.8$ and $\omega_{pl} = 1.6$. Starting from a random gas configuration small peptide–lipid aggregates quickly form, which over time fuse into progressively larger aggregates of varying sizes. All snapshots are from the same view direction.

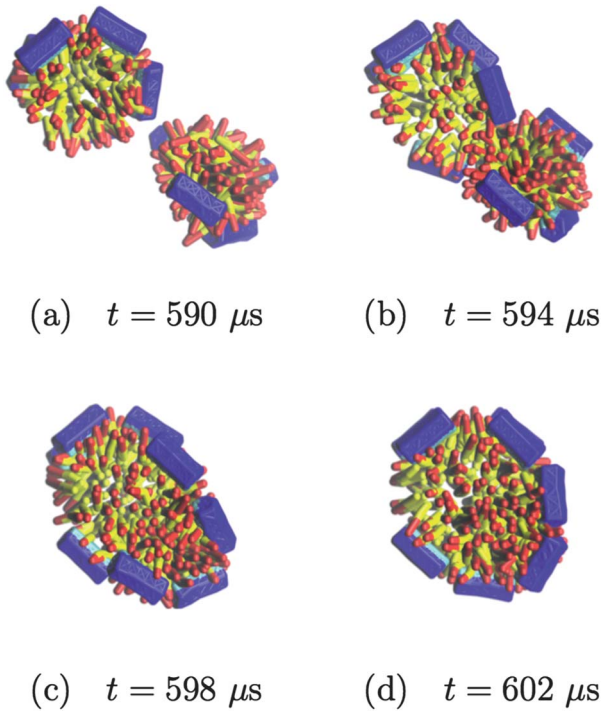

Fig. 4 Sequential snapshots showing the fusion between two small peptide–lipid aggregates forming a more well-defined discoidal aggregate. All images are along the same view direction and taken 4 μs apart. Data from simulations with interactions $\omega_{pp} = 0.8$ and $\omega_{pl} = 1.6$.

with our light scattering measurements. Also, as presented later, a polydisperse ensemble of disc structures proved to be necessary to fit the scattering data properly, the implementation of which is thus justified by the simulations.

The variation of the direct peptide–peptide interactions influences the aggregates formed and in particular whether or not peptide oligomers not associated with lipid discs are formed. In Fig. 4, a case with relatively low peptide–peptide interactions was shown and in that case practically all peptides are associated with a discoidal aggregate and are mostly arranged in pairs with their long axis along the disc perimeter. Raising ω_{pp} first introduces the formation of free oligomers in solution, typically trimers occasionally with a few lipids associated as shown in Fig. 5(a). As the peptide–peptide interaction becomes stronger than the peptide–lipid interaction, these peptide oligomers start forming fibre-like aggregates (see Fig. 5(b)) together with partly peptide saturated bicelles. When there are no direct peptide–peptide interactions, $\omega_{pp} = 0$, discoidal aggregates are still formed, but the peptides are located more randomly around the disc rim (not shown), *i.e.* the peptide pairing does not happen, illustrating that direct peptide–peptide interactions are required to form a well-defined peptide rim.

The structural model for analyzing the small-angle angle scattering data was refined based on the information obtained in the molecular dynamics simulations, which indicated both the polydispersity of the formed discs and the presence of trimers. No indications of peptide fibre-like structures were observed in the experimental data and it was concluded that the peptide–peptide and lipid–peptide interactions are comparable in the experimental system under the chosen conditions.

3.1.2 Size exclusion chromatography (SEC) data. Initial inspection of the SEC data (Fig. 6) reveals a relatively symmetrical and narrow peak. This implies the formation of particles that are monodisperse within the resolution of the column. It is also clearly visible that initial overnight incubation of the sample at 37 °C has a pronounced effect on the assembly of 18A:DMPC and gives rise to a more narrow distribution of species.

3.1.3 Time-resolved light scattering. Due to the dynamic nature of the system as seen in both the simulations and the time-coarse X-ray scattering data (data not shown), a light scattering study was performed to assess the evolution of the system over time (Fig. 7). From the light scattering data, it is evident that the gradual increase in the mass of the discs is influenced by the storage temperature of the sample. The growth-rate can be greatly reduced by lowering the storage temperature.

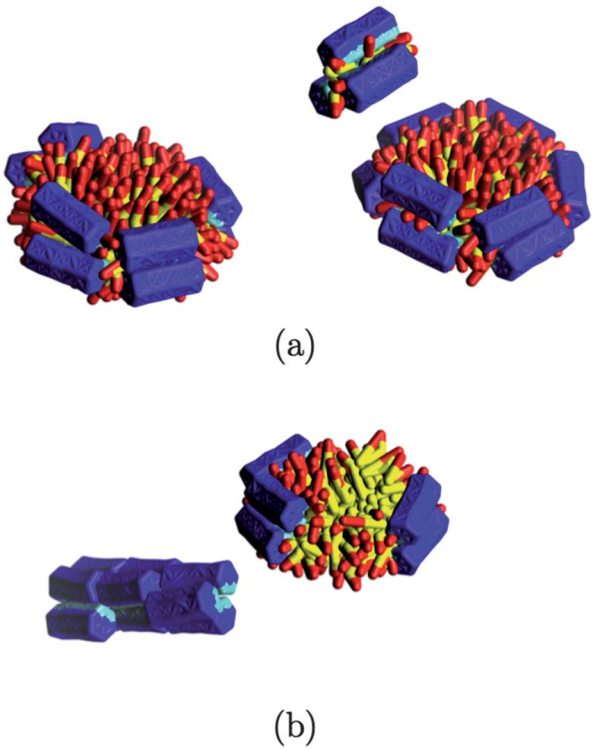

Fig. 5 Close-ups of aggregates formed in two different simulations. (a) Two discoidal aggregates and a peptide trimer formed in a system with interactions $\omega_{pp} = 1.2$ and $\omega_{pl} = 1.6$. The peptides preferably line the rim of the disc in aligned pairs. (b) A partly peptide saturated disc and peptide trimers forming a longer fibre-like aggregate in a system with interactions $\omega_{pp} = 1.6$ and $\omega_{pl} = 1.4$.

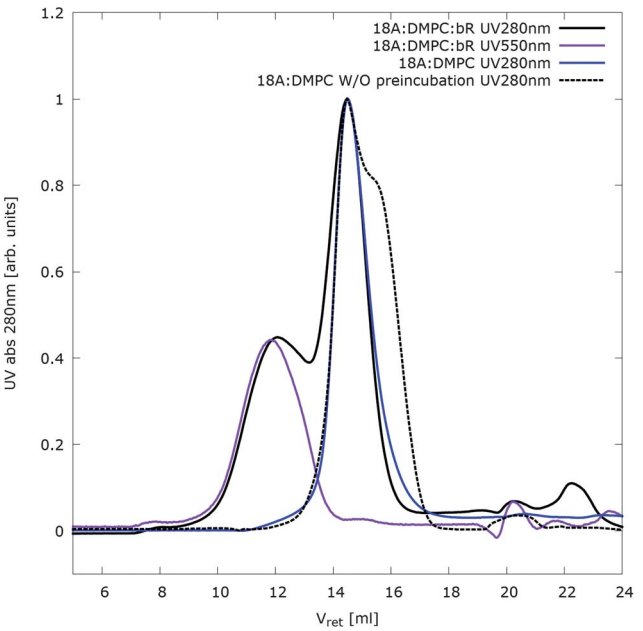

Fig. 6 SEC profiles on a Superdex 200 column of different 18A samples. The UV absorbance at 280 nm is plotted as a function of retention volume (V_{ret}) of the sample. Notice the importance of incubating the empty discs overnight at 37 °C in order to obtain a more monodisperse sample of the empty discs. Another important feature is that the size of the 18A:DMPC:bR discs is larger than the 18A:DMPC discs.

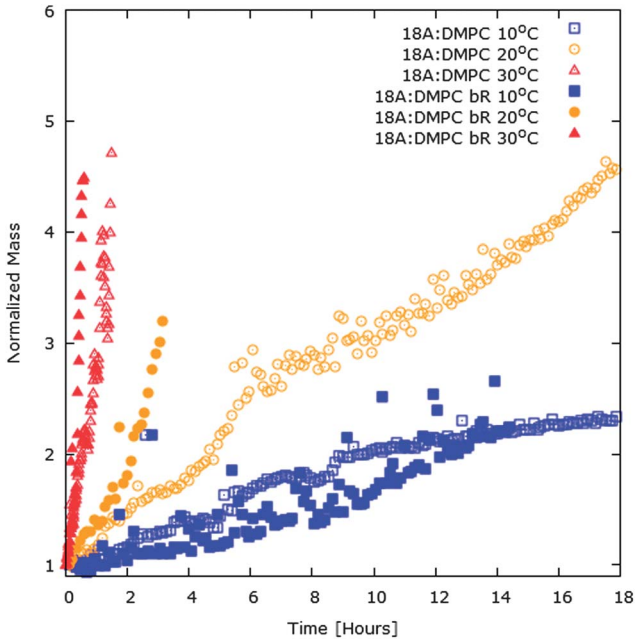

Fig. 7 The normalized mass as a function of time of the 18A:DMPC (empty symbols) and 18A:DMPC:bR (filled symbols) discs as a function of time measured by static light scattering. The mass is normalized by the initial particle mass, revealing the plotted normalized mass.

As described in the Materials and methods section, the SLS intensity was followed until the DLS measurements yielded a particle size of ~30 nm. Assuming that the stoichiometry of the particles is conserved to first order, the normalized intensity monitored by the SLS is directly proportional to the mass of the particle. From the data (see Fig. 7), we observe that the particles stored at 20 °C and 30 °C exhibit an increase in mass of 3–5 times before they reach a size of 30 nm, while the particles stored at 10 °C only exhibit an increase in mass of ~2 times, before they reach the same size. This indicates that particle aggregates of different overall geometries are formed depending on the temperature of the system.

3.1.4 Small-angle scattering

Initial analysis of the SAXS/SANS data. From a visual inspection of the scattering data (Fig. 8) a minimum around 0.08 $Å^{-1}$ is observed in the SAXS contrast. This arises from the oscillating contrast situation with positive excess scattering length density from the peptides and lipid headgroups and negative excess scattering length density from the alkyl tails of the lipids. In the neutron experiment, all excess scattering length densities are negative, which gives rise to a more bulk-like contrast resulting in a monotonically decaying intensity profile (Fig. 8).

Pair-distance distribution functions, $p(r)$, were obtained by using the Bayesian Indirect Fourier Transformation approach (BIFT).[62–64] The maximum interparticle distance found in the BIFT gives the size of the particle with much higher resolution and accuracy than found by SEC. As seen in Fig. 8, both SAXS and SANS data indicate a particle size of ~10 nm. Due to the bulk contrast of the SANS experiment, the shape of the $p(r)$ function gives the initial information of the overall structure of the particle. As seen in Fig. 8, the nearly bell-shaped $p(r)$ hints

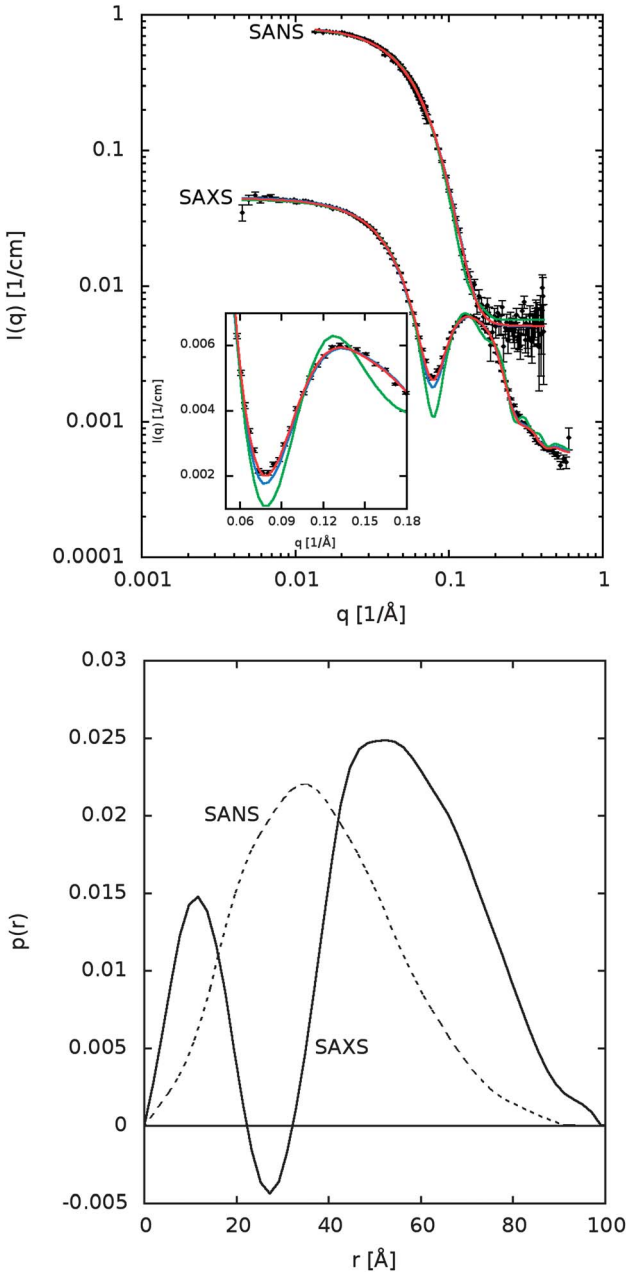

Fig. 8 Top: SANS and SAXS data (black points) with the corresponding fits (colored lines) plotted as the scattering intensity (I) as a function of the scattering vector (q). The colored lines represent different models that have been fitted to the experimental data. In green, a totally monodisperse sample is assumed. In blue, a polydisperse sample is assumed, while the red fit is a model including a small population of peptide trimers. Bottom: derived pair distance distribution functions of the data, obtained using the Bayesian approach for IFT.[64]

towards a compact particle that is not highly elongated, which in turn corresponds well with the shape of a discoidal particle. The different signs of the contrast of chains and headgroups in the lipids when investigated with X-rays are also reflected in the SAXS $p(r)$ function, where a negative minimum around 25 Å is observed. By using the BIFT software[64] we also obtain an estimate of the number of structural parameters extractable from the available experimental data. The models (see Section 2.2.1) applied in the later analysis are designed to have considerable fewer parameters ensuring a reliable analysis.

To move beyond the limited resolution of SEC, the polydispersity of the sample was further investigated by performing SAXS measurements on all collected fractions across the SEC peak (SAXS data not shown). This indeed confirmed that the discs in the sample were inherently slightly polydisperse and that SEC was not able to fully resolve this polydispersity. To ensure that similar ensembles of particles were measured by SAXS and SANS, we split one freshly prepared sample from the peak fraction of the SEC into two and performed simultaneous neutron and X-ray measurements. The success of this approach is confirmed by the similar size of the particles observed by SAXS and SANS (Fig. 8, lower panel).

Model based analysis of SAXS and SANS data. The proposed model for the 18A:DMPC discs (described in Computational methods, see Fig. 1) was simultaneously fitted to the SAXS/SANS data presented in Fig. 8. This exploits the information on the different contrast situations observed by SAXS and SANS. Data and associated fits are plotted in the same figure. Three different fits are presented, each representing models of the system with increasing complexity. The fit based on the most simple model, which is a fully monodisperse population of discs and no peptide trimers, is shown in green. This fit has a $\chi^2 = 20.4$ and clearly fails to reproduce the finer details in the experimental data. The second fit assumes a polydisperse disc population, is shown in blue and has a $\chi^2 = 3.88$. As the χ^2 value indicates, this model fits the experimental data much better. The third fit seen in red is a model of polydisperse discs with a small population of peptide trimers, which results in a $\chi^2 = 3.23$. The small gain in the χ^2 value comes at the expense of an additional parameter in the model, which is the ratio between peptides and lipids in the entire sample. The values of the fitted parameters did not differ significantly between the two best fits even though the minimum in the SAXS data is clearly better fitted when including the trimer.

The introduction of the polydispersity lowered the χ^2 remarkably at the cost of a single fitting parameter, which, in combination with simulation results, was deemed significant to adopt in our final model. Furthermore, in a dynamic system such as the 18A:DMPC system, a degree of polydispersity is to be expected.[28] Initially, one notices a good agreement in the ranges of q smaller than 0.05 $Å^{-1}$ – corresponding to a good description of the overall particle size and size distribution. The fit reproduces the characteristic features in the intermediate q-range from 0.05 $Å^{-1}$ to 0.25 $Å^{-1}$ in the data, suggesting that the actual model of the disc and the bilayer is an adequate description of the system in the context of the small-angle scattering resolution. From 0.25 $Å^{-1}$ and higher values of q, the model gives an increasingly poor description of the SAXS data. This is to be expected, as the geometrical model is too simple to adequately describe the local structure described in this range of the momentum transfer.

Model fit results. The refined values for the fitted and derived parameters from the polydisperse model with added trimers are listed in Table 2. Apart from the presented parameters, a

Table 2 Values and uncertainties for model parameters refined from the presented fit as well as parameters derived from the refined parameters

Refined parameter	Value	Confidence interval – 95%	Derived parameters	Value
Mean number of lipids per disc, $\bar{n}$	113	104–122	Mean number of peptides per disc, η	17.1
Std. dev. of distribution, σ	40.7	26.7–63.3	Bilayer thickness	42.3 Å
Area per lipid headgroup, a_{head}	52.1 Å^2	49.2 Å^2–54.9 Å^2	Hydrophobic bilayer thickness	30.1 Å
Width of the peptide belt, d	8.10 Å	7.00 Å–9.22 Å	Methyl layer thickness	4.13 Å
Volume of a single peptide, ν_p	2430 Å^3	2330 Å^3–2540 Å^3	Length of the peptide trimer, l	31.0 Å
Volume of a single lipid, ν_l	1100 Å^3	1080 Å^3–1120 Å^3	Fraction of peptides in trimers	0.0925
Lipid–peptide in the sample, φ	7.51	6.08–8.65		

constant background was fitted along with an interface roughness parameter, accounting for a more physically realistic smearing of the otherwise infinitely sharp interfaces in the model. We observe that all the obtained values of the refined parameters are consistent with our expectations. In particular, we find that the parameters describing the lipids, the mean number of lipids per disc, $\bar{n}$, the area per lipid headgroup, a_{head}, and the volume of a lipid, ν_l, all exhibit a low relative uncertainty. This highlights the strength of this combination of techniques. On the other hand, the width of the Gauss distribution, σ, is determined relatively poorly by this method. The width of the peptide belt, d, is fitted to a value (8.1 Å) that corresponds very well with the expected diameter of an α helix. This is in agreement with the proposed structure of the peptides located on the perimeter of the disc. The overall partial specific molecular volume of the peptide is slightly lower than anticipated; however, the uncertainty in this quantity is considerably larger than that of the corresponding volume of the lipids. Apart from the presented fitting parameters, a list of derived parameters, inferred from the model fit, is also included in Table 2. The values of the derived parameters describing the bilayer are very much in line with our expectations for the structure of a DMPC-bilayer as the area per headgroup matches the values found in the literature.[65]

3.2 The 18A:DMPC:bR system

3.2.1 SEC data. From the SEC profile obtained for the 18A:DMPC:bR discs (Fig. 6), we observe that they have a shorter retention time on the column than the 18A:DMPC discs, indicating a larger particle size. Furthermore, by monitoring the specific bR absorbance, it is clear that the column has sufficient resolving power to provide a good separation of the bR containing discs from the empty ones.

3.2.2 SAXS data. The obtained SAXS data of the 18A:DMPC:bR particles are plotted together with the corresponding $p(r)$-function in Fig. 9. An initial inspection of the scattering data revealed that there was a clear minimum around 0.08 Å^{-1}, very similar to the empty 18A:DMPC discs. This oscillation stems, as with the 18A:DMPC discs, from the oscillating contrast situation of the lipids and the proteins when compared to the solvent. Looking at the $p(r)$ function, the minimum at 25 Å is less pronounced than the one observed in the SAXS contrast for the empty 18A:DMPC discs. Considering the constituents of the particle, this is a good indication that bR

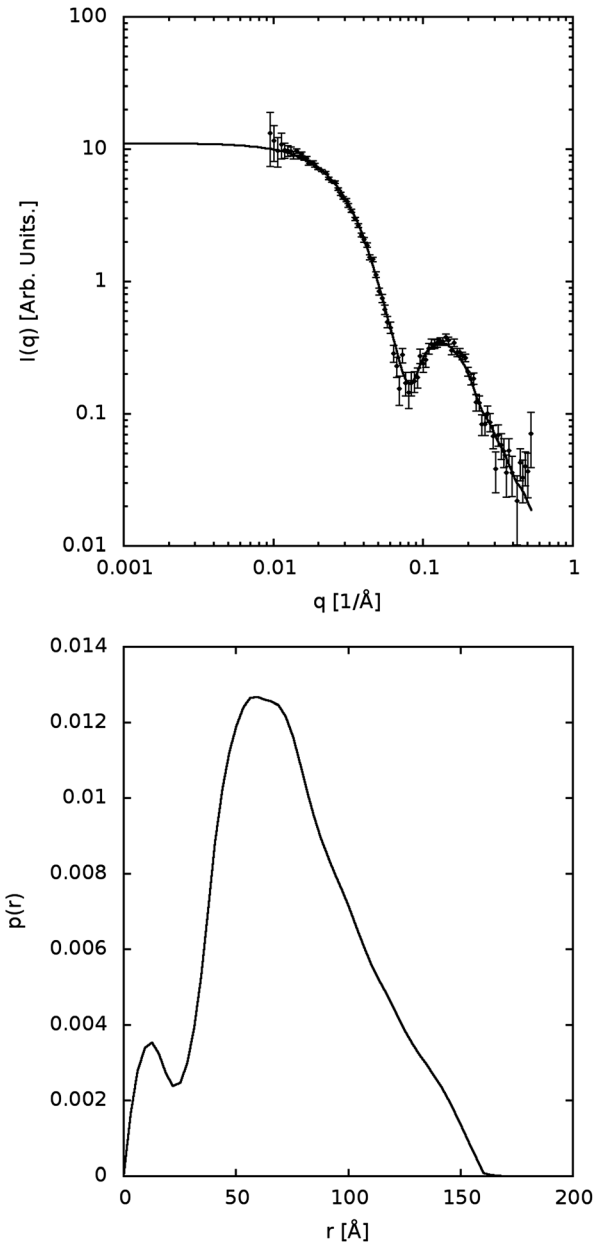

Fig. 9 Top: SAXS data (points) obtained for the 18A:DMPC:bR discs along with the corresponding IFT fit (full line). The scattering intensity (I) is plotted as a function of the scattering vector (q). Bottom: the indirect Fourier transform (IFT) of the data. The maximum distance between the particles (D_{max}) is observed to be ~17 nm.

is situated in the discs. The shape of the $p(r)$ function indicates a compact and definitely not elongated particle shape, as with the 18A:DMPC $p(r)$ function, corresponding well to a discoidal shaped particle. The D_{max} found by the BIFT shows a maximum size of the particles to be ~17 nm. This corresponds well with DLS measurements (D = 17 nm), and the larger size of the particles in comparison with the empty 18A:DMPC discs as observed by SEC. The polydispersity of the sample was investigated by SAXS measurements on all fractions collected from the bR containing SEC peak (data not shown). This revealed that the SEC peak contained different sized particles as also observed in the peak of the empty discs.

3.2.3 Stability of bacteriorhodopsin in 18A:DMPC discs. The stability of bR in detergent and 18A:DMPC discs was monitored over time at 4 °C and 20 °C. The results are shown in Fig. 10. It is evident that cooling the sample has a positive effect on the lifetime of bR. But it is also clearly observed that the bR is more stable in 18A discs than in OG. The black crosses in Fig. 10 represent the point in time, where the samples became turbid.

This highlights the advantage of using 18A:DMPC particles over detergents, when it is necessary to work with membrane proteins over long periods of time. An interesting point is the fact that bR stabilized in 18A:DMPC particles remained characteristically purple for months after the samples turned turbid, even at 20 °C and shows that the 18A:DMPC particles have a highly stabilizing effect on bR, even though the size of the discs evolves over time according to the SLS data (Fig. 7). It is observed that the 18A:DMPC:bR discs have approximately the same time and temperature dependence of the growth rate as

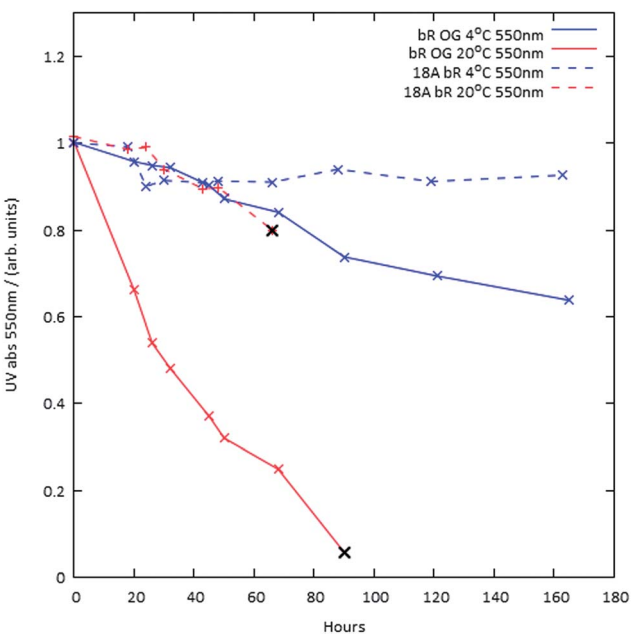

Fig. 10 UV absorption measurements at 550 nm as a function of time, quantifying the stability of bR in 18A:DMPC discs and the detergent OG at different temperatures. The black crosses (*X*) represent the point, when samples became turbid, and light scattering was interfering with the absorption measurements.

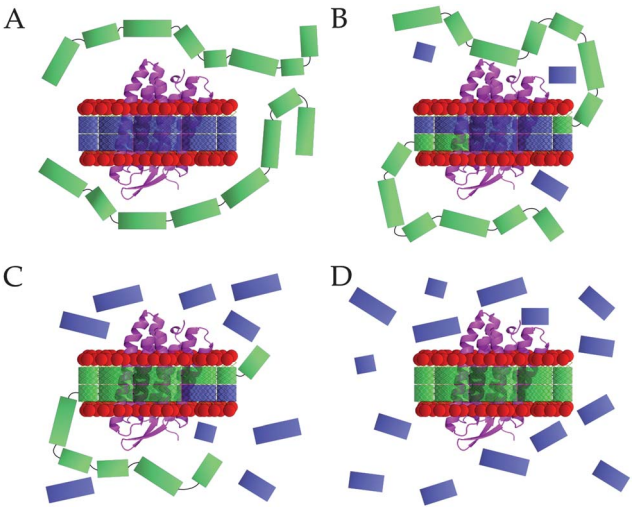

Fig. 11 Schematic representation of the transfer of bR and DMPC from the 18A discs to the MSP1D1 based discs. Purified MSP1D1 was added to the 18A:DMPC:bR discs and left to exchange at room temperature for one hour.

the 18A:DMPC discs. The incorporation of bR into the discs does, however, seem to destabilize the 18A:DMPC system, as evidenced by the slightly elevated growth-rate of the 18A:DMPC:bR discs (observed at 20 °C and 30 °C in Fig. 7).

3.3 Transfer of bacteriorhodopsin from 18A:DMPC:bR to nanodiscs

Very interestingly, the dynamic nature of the 18A peptide nanodisc allows the replacement of the 18A peptides with the longer MSP1D1. This means that the 18A:DMPC particles can be used as an intermediate step in the process of transferring membrane proteins into nanodiscs, hence greatly reducing the exposure to detergents.

The strategy of the transfer is outlined in Fig. 11. As described in the Experimental methods, the MSP1D1 protein belts were added to the purified 18A:DMPC:bR discs, and it was observed that they replaced the 18A peptides, thereby incorporating both the membrane protein and the phospholipids directly from the peptide based discs. After the exchange, the MSP1D1:DMPC:bR discs were purified by affinity chromatography utilizing the His-tag on the MSP1D1 belt. This ensured that no 18A discs were retained in the sample. Afterwards, the obtained sample was characterized by SEC and SDS-PAGE (data not shown) to ensure that they consisted of MSP1D1 and bR and had a hydrodynamic radius similar to that of the empty DMPC:MSP1D1 nanodiscs. The SDS-PAGE showed that the major protein species were bR and MSP1D1. The SEC profile exhibited a retention time of the MSP1D1:DMPC:bR very similar to the empty MSP1D1 discs, indicating that the two particles have a similar size. The retention time on the SEC column was not expected to change much as compared to that of the empty MSP1D1 based nanodiscs, since bR is primarily buried in the phospholipid bilayer and therefore should not significantly influence the hydrodynamic radius of the particle.

4 General discussion

4.1 The 18A:DMPC nanodiscs

The combined analysis of SAXS/SANS-data shows that the 18A:DMPC system forms disc shaped particles with a diameter of ~10 nm and some polydispersity. The observation of ~10 nm particles is supported by dynamic light scattering. Apart from providing information about the overall shape and size of the discs, the combination of SAXS/SANS allows for extracting more detailed structural information about the discs. In the modeled distribution, the most frequent disc size – often referred to as the mode of the distribution – contained 113 lipids and 17.5 peptides corresponding to a radius of the bilayer patch of 30.7 Å. This makes these empty 18A discs slightly smaller than the ApoA1-based discs.[26] The area per lipid headgroup was refined to ~52 Å^2 when situated in the empty 18A discs and measured at 20 °C. This value falls well within the previously described gel-phase value of 47.2 ± 0.5 Å^2 measured at 15 °C[66] and the fluid phase value of 59.9 ± 1.2 Å^2 measured at 30 °C.[67]

The SAXS/SANS analysis also clearly showed that the 18A:DMPC stoichiometry of the formed discs was altered compared to the stoichiometry of the initial mixture. In the investigated preparations, only about 50% of the 18A peptides contributed to the formation of discs, while the rest of the peptides formed smaller particles and were removed in the initial SEC based purification step.

The finding of the discoidal structure is consistent with an interesting, previously reported SEC and NMR study.[19] Here, SEC was used to determine the size of the discs, and a disc diameter of 6.9 nm was estimated, while NMR was used to prove that the lipid alkyl chains and the peptides were oriented perpendicular to each other. The combined information was in good agreement with the assumption of a discoidal shaped particle. By further assuming a DMPC area per headgroup of 70 Å^2, the authors proposed a model for disc shaped particles each composed of 16 peptides and 54 DMPC's.[19] However, it is clear that even when adjusting for a too high value of the area per headgroup for DMPC assumed in the previous study,[19] this SEC based estimate provides a value for the size and stoichiometry of the disc that is significantly lower than the one we observed.

A static light scattering analysis of the system showed that the discs observed in the 18A:DMPC system are only in a metastable state. The average size of the discs increased significantly as a function of time, and the growth rate was elevated at higher temperatures. In order to obtain a consistent snapshot of the formed structure, it became very beneficial to have access to fully simultaneous SAXS and SANS measurements of the samples. The fact that the first DLS measurements were made immediately after purification of the 18A:DMPC nanodiscs provided a good measurement of the initial particle size. The SAXS and SANS measurements were also made immediately after purification and revealed a disc size similar to what was observed in the first DLS measurement points.

A coarse-grained molecular dynamics simulation approach mimicked and predicted the overall characteristics of the system. This provided very useful feedback for the modeling of the scattering data. Although this approach has been used to study peptide–lipid interactions before,[59] disc formation has not been reported until the present study. The experimental findings for the empty 18A:DMPC discs are in qualitative agreement with these coarse-grained computer simulations. In the present study, the interaction parameter phase space was searched in order to identify the regions, in which disc-shaped structures actually formed. It is interesting to observe how small adjustments of the interaction parameters gave rise to different self-assembly behaviours. This finding is consistent with the observation of a visible temperature dependence of the experimental system as observed from the light scattering data.

4.2 The 18A:DMPC:bR nanodiscs

The present study examines for the first time the experimental potential of the 18A:DMPC discs as a tool for handling and stabilizing membrane proteins. Preparation of 18A:DMPC:bR discs was found to be remarkably simple and highly experimentally reproducible.

The advantage of the 18A:DMPC nanodiscs in stabilizing bR is evident from the superior stability of bR in the 18A:DMPC discs compared to OG micelles (see Fig. 10). The stability was conserved over extremely long periods of time (several months) despite the fact that the size of the 18ADMPC:bR particles increased. While this increased stability is fully compatible with the fact that the DMPC bilayer provides a more native-like environment for bR than a detergent micelle, the effect of changing to this still relatively simple alternative system has nevertheless not been explored until now.

The formed 18A:DMPC:bR discs exhibited an initial size of ~17 nm as determined from the SAXS $p(r)$ function and, like the 18A:DMPC system, the 18A:DMPC:bR discs exhibited some degree of polydispersity as judged from the SAXS analysis of the single SEC fractions.

In the present study, we have also demonstrated that the 18A:DMPC system can be used as an intermediate step on the way from detergent solubilized membrane proteins to membrane proteins stabilized in nanodiscs. It was possible to transfer the membrane protein from a detergent solubilized state, through the stabilizing 18A:DMPC discs and to a MSP1D1-based nanodisc. This is important as it, for some membrane protein complexes, is difficult to transfer directly from the reconstitution detergents to the MSP1D1-based discs. The extra flexibility obtained by means of this 18A:DMPC system may become an important tool for optimal handling and reconstitution of membrane proteins.

We did not attempt to simulate the more complex 18A:DMPC:bR system with the coarse-grained molecular dynamics approach in the present study. However, it is obvious that further development of the coarse-grained simulation tools in this direction could provide a very powerful tool for the exploration of the self-assembly behavior of the combined system and for predicting the effect of incorporating membrane proteins into different discoidal systems.

5 Conclusion and perspectives

In this study, we have performed detailed characterization of 18A:DMPC discoidal lipoprotein-like particles with a range of structural methods. This characterization is backed up by coarse-grained molecular dynamics simulations. The particles were consistently shown to have a flat discoidal structure with some polydispersity. The size of the discs evolved over time, relatively fast at high temperatures and significantly slower at low temperatures. These experimental findings are fully supported by coarse-grained computer simulations.

It is shown for the first time that the 18A peptide can be used for stabilizing and handling a membrane protein, in the present case bacteriorhodopsin. Importantly, we find that the membrane protein has a significantly increased stability in the 18A:DMPC discs compared to that in a traditional mild reconstitution detergent. This may be a result of the dynamic sampling of different disc sizes formed in the 18A:DMPC system. This allows for a thermodynamically optimal match between the structure of the membrane protein and the size of the surrounding disc.

Finally, we show that the 18A:DMPC discs can be used as an intermediate platform for membrane proteins between a detergent micelle and a MSP1D1-based nanodisc. We believe that this gives the system important potential for the handling and stabilization of membrane proteins.

All together, we believe that the 18A:DMPC system in particular and this type of peptide–phospholipid system more generally are very promising for solution handling of membrane proteins, but also for high resolution structural studies such as NMR and membrane protein crystallography. However, unlike similar systems, these peptide-based disc systems are still only very sparsely investigated and described in the scientific literature.

Acknowledgements

The authors would like to thank Dr A. Round at the ID14-3 BioSAXS beamline at ESRF, the European Synchrotron Radiation Facility, and Dr R. Schweins at the SANS instrument at the beamline D11 at ILL, Institute Laue Langevin. We gratefully acknowledge the possibility for obtaining truly simultaneous SAXS and SANS data at the ILL and ESRF. The authors thank Dr T. Plivelic at the I911-4 beamline at Max-lab, the national Swedish synchrotron facility. Finally, we thank the Danish Government funded UNIK Synthetic Biology program, The Lundbeck Foundation, Danscatt as well as the McXtrace-project for co-funding of the project.

References

1 L. Fagerberg, K. Jonasson, G. von Heijne, M. Uhlén and L. Berglund, *Proteomics*, 2010, **10**, 1141–1149.
2 M. A. Yildirim, K.-I. Goh, M. E. Cusick, A.-L. Barabási and M. Vidal, *Nat. Biotechnol.*, 2007, **25**, 1119–1126.
3 S. R. G. F. Rasmussen, B. T. DeVree, Y. Zou, A. C. Kruse, K. Y. Chung, T. S. Kobilka, F. S. Thian, P. S. Chae, E. Pardon, D. Calinski, J. M. Mathiesen, S. T. a. Shah, J. a. Lyons, M. Caffrey, S. H. Gellman, J. Steyaert, G. Skiniotis, W. I. Weis, R. K. Sunahara and B. K. Kobilka, *Nature*, 2011, **477**, 549–555.
4 A. Buffet, A. Rothkirch, R. Döhrmann, V. Körstgens, M. M. Abul Kashem, J. Perlich, G. Herzog, M. Schwartzkopf, R. Gehrke, P. Müller-Buschbaum and S. V. Roth, *J. Synchrotron Radiat.*, 2012, **19**, 647–653.
5 S. Cusack, H. Belrhali, a. Bram, M. Burghammer, a. Perrakis and C. Riekel, *Nat. Struct. Biol.*, 1998, **5**, 634–637.
6 R. F. Fischetti, S. Xu, D. W. Yoder, M. Becker, V. Nagarajan, R. Sanishvili, M. C. Hilgart, S. Stepanov, O. Makarov and J. L. Smith, *J. Synchrotron Radiat.*, 2009, **16**, 217–225.
7 T. K. Ritchie, Y. V. Grinkova, T. H. Bayburt, I. G. Denisov, J. K. Zolnerciks, W. M. Atkins and S. G. Sligar, *Reconstitution of membrane proteins in phospholipid bilayer nanodiscs*, Elsevier Inc., 1st edn, 2009, vol. 464, ch. 11, pp. 211–231.
8 P. Linsel-Nitschke and A. R. Tall, *Nat. Rev. Drug Discovery*, 2005, **4**, 193–205.
9 J.-C. Tardif, J. Grégoire, P. L. L'Allier, R. Ibrahim, J. Lespérance, T. M. Heinonen, S. Kouz, C. Berry, R. Basser, M.-A. Lavoie, M.-C. Guertin and J. Rodés-Cabau, *JAMA, J. Am. Med. Assoc.*, 2007, **297**, 1675–1682.
10 G. M. Anantharamaiah, J. L. Jones, C. G. Brouillette, C. F. Schmidt, B. H. Chung, T. A. Hughes, A. S. Bhown and J. P. Segrest, *J. Biol. Chem.*, 1985, **260**, 10248–10255.
11 C. Beaufils, C. Alexopoulos, M. P. Petraki, A. D. Tselepis, N. Coudevylle, M. Sakarellos-daitsiotis, C. Sakarellos, M. T. Cung and N. Cedex, *Biopolymers*, 2006, **88**, 362–372.
12 M. Nikanjam, E. a. Blakely, K. a. Bjornstad, X. Shu, T. F. Budinger and T. M. Forte, *Int. J. Pharm.*, 2007, **328**, 86–94.
13 M. Tanaka, T. Tanaka, S. Ohta, T. Kawakami, H. Konno, K. Akaji, S. Aimoto and H. Saito, *J. Pep. Sci.*, 2009, **15**, 36–42.
14 G. D. Wool, C. a. Reardon and G. S. Getz, *J. Lipid Res.*, 2008, **49**, 1268–1283.
15 M. Navab, *Circulation*, 2002, **105**, 290–292.
16 L. T. Bloedon, R. Dunbar, D. Duffy, P. Pinell-Salles, R. Norris, B. J. DeGroot, R. Movva, M. Navab, A. M. Fogelman and D. J. Rader, *J. Lipid Res.*, 2008, **49**, 1344–1352.
17 C. G. Brouillette, J. L. Jones, T. C. Ng, H. Kercret, B. H. Chung and J. P. Segrest, *Biochemistry*, 1984, **23**, 359–367.
18 B. H. Chung, G. M. Anatharamaiah, C. G. Brouillette, T. Nishida and J. P. Segrest, *J. Biol. Chem.*, 1985, **260**, 10256–10262.
19 V. K. Mishra, G. M. Anantharamaiah, J. P. Segrest, M. N. Palgunachari, M. Chaddha, S. W. S. Sham and N. R. Krishna, *J. Biol. Chem.*, 2006, **281**, 6511–6519.
20 V. K. Mishra, M. N. Palgunachari, R. Krishna, J. Glushka, J. P. Segrest and G. M. Anantharamaiah, *J. Biol. Chem.*, 2008, **283**, 34393–34402.
21 J. P. Segrest, H. De Loof, J. G. Dohlman, C. G. Brouillette and G. M. Anantharamaiah, *Proteins*, 1990, **8**, 103–117.
22 D. Bashtovyy, M. K. Jones, G. M. Anantharamaiah and J. P. Segrest, *J. Lipid Res.*, 2011, **52**, 435–450.
23 K. Müller, *Biochemistry*, 1981, **20**, 404–414.

24 S. Faham and J. U. Bowie, *J. Mol. Biol.*, 2002, **316**, 1–6.
25 S. R. G. F. Rasmussen, H.-J. Choi, D. M. Rosenbaum, T. S. Kobilka, F. S. Thian, P. C. Edwards, M. Burghammer, V. R. P. Ratnala, R. Sanishvili, R. F. Fischetti, G. F. X. Schertler, W. I. Weis and B. K. Kobilka, *Nature*, 2007, **450**, 383–387.
26 T. H. Bayburt, Y. V. Grinkova and S. G. Sligar, *Nano Lett.*, 2002, **2**, 853–856.
27 T. H. Bayburt and S. G. Sligar, *FEBS Lett.*, 2010, **584**, 1721–1727.
28 J. N. Israelachvili, *Intermolecular and Surface Forces*, Ademic Press – Elsevier, 3rd edn, 2011.
29 N. R. Civjan, T. H. Bayburt, M. a. Schuler and S. G. Sligar, *BioTechniques*, 2003, **35**, 556–560.
30 C. E. Schafmeister, L. J. Miercke and R. M. Stroud, *Science*, 1993, **262**, 734–738.
31 X. Zhao, Y. Nagai, P. J. Reeves, P. Kiley, H. G. Khorana and S. Zhang, *Proc. Natl. Acad. Sci. U. S. A.*, 2006, **103**, 17707–17712.
32 X. Wang, K. Corin, P. Baaske, C. J. Wienken, M. Jerabek-Willemsen, S. Duhr, D. Braun and S. Zhang, *Proc. Natl. Acad. Sci. U. S. A.*, 2011, **108**, 9049–9054.
33 P. Kiley, X. Zhao, M. Vaughn, M. a. Baldo, B. D. Bruce and S. Zhang, *PLoS Biol.*, 2005, **3**, e230.
34 K. Corin, P. Baaske, D. B. Ravel, J. Song, E. Brown, X. Wang, C. J. Wienken, M. Jerabek-Willemsen, S. Duhr, Y. Luo, D. Braun and S. Zhang, *PLoS One*, 2011, **6**, e25067.
35 J. I. Yeh, S. Du, A. Tortajada, J. Paulo and S. Zhang, *Biochemistry*, 2005, **44**, 16912–16919.
36 K. Matsumoto, M. Vaughn, B. D. Bruce, S. Koutsopoulos and S. Zhang, *J. Phys. Chem. B*, 2009, **113**, 75–83.
37 J.-L. Popot, T. Althoff, D. Bagnard, J.-L. Banères, P. Bazzacco, E. Billon-Denis, L. J. Catoire, P. Champeil, D. Charvolin, M. J. Cocco, G. Crémel, T. Dahmane, L. M. de la Maza, C. Ebel, F. Gabel, F. Giusti, Y. Gohon, E. Goormaghtigh, E. Guittet, J. H. Kleinschmidt, W. Kühlbrandt, C. Le Bon, K. L. Martinez, M. Picard, B. Pucci, J. N. Sachs, C. Tribet, C. van Heijenoort, F. Wien, F. Zito and M. Zoonens, *Annu. Rev. Biophys.*, 2011, **40**, 379–408.
38 C. Tribet, R. Audebert and J.-L. Popot, *Langmuir*, 1997, **13**, 5570–5576.
39 Y. V. Venkatachalapathi, M. C. Phillips, R. M. Epand, R. F. Epand, E. M. Tytler, J. P. Segrest and G. M. Anantharamaiah, *Proteins*, 1993, **15**, 349–359.
40 G. Datta, M. Chaddha, S. Hama, M. Navab, a. M. Fogelman, D. W. Garber, V. K. Mishra, R. M. Epand, R. F. Epand, S. Lund-Katz, M. C. Phillips, J. P. Segrest and G. M. Anantharamaiah, *J. Lipid Res.*, 2001, **42**, 1096–1104.
41 D. Oesterhelt and W. Stoeckenius, *Methods Enzymol.*, 1974, **31**, 667–678.
42 N. Dencher, *Methods Enzymol.*, 1982, **88**, 5–10.
43 V. A. Bloomfield, *Biopolymers*, 2000, **54**, 168–172.
44 S. Acton, a. Rigotti, K. T. Landschulz, S. Xu, H. H. Hobbs and M. Krieger, *Science*, 1996, **271**, 518–520.
45 N. Skar-Gislinge, J. B. Simonsen, K. Mortensen, R. Feidenhans'l, S. G. Sligar, B. Lindberg Møller, T. Bjø rnholm and L. Arleth, *J. Am. Chem. Soc.*, 2010, **132**, 13713–13722.
46 N. Skar-Gislinge and L. Arleth, *Phys. Chem. Chem. Phys.*, 2011, **13**, 3161–3170.
47 J. S. Pedersen, *Adv. Colloid Interface Sci.*, 1997, **70**, 171–210.
48 D. Marquardt, *J. Soc. Ind. Appl. Math.*, 1963, **11**, 431–441.
49 W. S. J. Nocedal, *Numerical Optimization*, Springer, 1999.
50 C. G. Broyden, *IMA J. Appl. Math.*, 1970, **6**, 76–90.
51 R. Fletcher, *Comput. J.*, 1970, **13**, 317–322.
52 D. Goldfarb, *Math. Comp.*, 1970, **24**, 23.
53 D. F. Shanno, *Math. Comp.*, 1970, **24**, 647.
54 E. Ziegel, W. Press, B. Flannery, S. Teukolsky and W. Vetterling, *Numerical Recipes*, The Art of Scientific Computing, 1987, vol. 29, p. 501.
55 P. Mittelbach and G. Porod, *Acta Phys. Austriaca*, 1961, **14**, 405–439.
56 I. R. Cooke and M. Deserno, *J. Chem. Phys.*, 2005, **123**, 1–13.
57 I. Cooke, K. Kremer and M. Deserno, *Phys. Rev. E: Stat., Nonlinear, Soft Matter Phys.*, 2005, **72**, 2–5.
58 B. J. Reynwar, G. Illya, V. A. Harmandaris, M. M. Müller, K. Kremer and M. Deserno, *Nature*, 2007, **447**, 461–464.
59 G. Illya and M. Deserno, *Biophys. J.*, 2008, **95**, 4163–4173.
60 H. J. Limbach, A. Arnold, B. A. Mann and C. Holm, *Comput. Phys. Commun.*, 2006, **174**, 704–727.
61 W. Humphrey, A. Dalke and K. Schulten, *J. Mol. Graphics*, 1996, **14**, 33.
62 O. Glatter, *J. Appl. Crystallogr.*, 1977, **10**, 415–421.
63 J. S. Pedersen, S. Hansen and R. Bauer, *Eur. Biophys. J*, 1994, **22**, 379–389.
64 S. Hansen, *J. Appl. Crystallogr.*, 2012, **45**, 566–567.
65 J. Pan, F. a. Heberle, S. Tristram-Nagle, M. Szymanski, M. Koepfinger, J. Katsaras and N. Kučerka, *Biochim. Biophys. Acta*, 2012, **1818**, 2135–2148.
66 S. Tristram-Nagle, Y. Liu, J. Legleiter and J. F. Nagle, *Biophys. J.*, 2002, **83**, 3324–3335.
67 N. Kučerka, M.-P. Nieh and J. Katsaras, *Biochim. Biophys. Acta*, 2011, **1808**, 2761–2771.

